LETTER

A topological source of quantum light

Sunil Mittal[1,2]*, Elizabeth A. Goldschmidt[1,3] & Mohammad Hafezi[1,2,4]

Quantum light is characterized by distinctive statistical distributions that are possible only because of quantum mechanical effects. For example, single photons and correlated photon pairs exhibit photon number distributions with variance lower than classically allowed limits. This enables high-fidelity transmission of quantum information and sensing with lower noise than possible with classical light sources[1,2]. Most quantum light sources rely on spontaneous parametric processes such as down-conversion and four-wave mixing[2]. These processes are mediated by vacuum fluctuations of the electromagnetic field. Therefore, by manipulating the electromagnetic mode structure, for example with dispersion-engineered nanophotonic systems, the spectrum of generated photons can be controlled[3–7]. However, disorder, which is ubiquitous in nanophotonic fabrication, causes device-to-device spectral variations[8–11]. Here we realize topologically robust electromagnetic modes and use their vacuum fluctuations to create a quantum light source in which the spectrum of generated photons is much less affected by fabrication-induced disorder. Specifically, we use the topological edge states realized in a two-dimensional array of ring resonators to generate correlated photon pairs by spontaneous four-wave mixing and show that they outperform their topologically trivial one-dimensional counterparts in terms of spectral robustness. We demonstrate the non-classical nature of the generated light and the realization of a robust source of heralded single photons by measuring the conditional antibunching of photons, that is, the reduced likelihood of photons arriving together compared to thermal or laser light. Such topological effects, which are unique to bosonic systems, could pave the way for the development of robust quantum photonic devices.

Spontaneous four-wave mixing (SFWM) is a third-order nonlinear process in which two pump photons at frequency ω_p are annihilated, and two daughter photons, called signal and idler, are generated at frequencies ω_s and ω_i. The spectra of the generated signal and idler photons as well as their correlations are dictated by energy and momentum conservation relations, $2\omega_p = \omega_s + \omega_i$ and $2k_p = k_s + k_i$, where k indicates the momenta of the respective fields. The spectrum is further constrained by the electromagnetic mode structure: that is, the density of states or, equivalently, the dispersion relation $\omega(k)$, which governs the propagation of the pump, signal and idler photons. Recently, the use of nanophotonic systems such as toroidal and ring resonators has provided a compact and scalable route to manipulate the electromagnetic mode structure and hence to implement spectrally engineered sources of correlated photons[2–4]. For example, coupled ring resonator arrays can be used to control the number of spectral modes[7] as well as to enhance the rate of photon pair generation, without compromising their bandwidth[6,12]. However, nanophotonic systems are invariably disposed to fabrication disorder, which can alter the dispersion of the photonic modes in an unpredictable fashion[8–10] and can result in randomness in the spectrum of photons generated by different devices. This randomness limits the scalability of such sources for practical applications in quantum communication and information processing, which often require multiple sources with identical spectra, for example in multi-photon interference[11].

At the same time, the introduction of topological protection in photonic systems has led to the development of a new class of devices that are inherently robust against disorder[13–19]. This robustness can be attributed to the presence of unidirectional, back-reflection-free edge states in these systems. Edge states are characterized by topologically invariant integers[20–22], and photonic transport through these states is therefore protected against local disorder[14,19,23]. Edge states have been used to demonstrate, for example, robust optical delay lines[16,23], reconfigurable photonic pathways[19] and topological lasers[24,25]. However, such demonstrations have so far been confined to the classical regime.

In this work, we use topology for spectral engineering of the quantum fluctuations of the electromagnetic vacuum and implement a robust source of correlated photon pairs generated by SFWM. In particular, we exploit the linear dispersion associated with edge states for efficient phase-matching and show that the photon pair generation is enhanced when the pump, as well as the signal and idler fields, corresponds to edge modes of the system. We demonstrate correlations between the signal and idler photons beyond what is possible with classical sources and show conditional antibunching of photons, confirming the quantum nature of our source and its operation as a source of heralded single photons. More importantly, using measurements over many devices, we show that the robustness of such topological spectral engineering manifests as a robustness in the spectrum of generated photons and that our topological source outperforms a similarly designed topologically trivial source of correlated photons. From a fundamental perspective, our scheme is similar to recent theoretical proposals[26,27] that investigated second- and third-order nonlinearity in topological edge states, respectively. These particle-non-conserving topological photonic systems have no fermionic counterparts.

Our system consists of a two-dimensional (2D) square lattice of ring resonators, positioned at the lattice sites, for which the non-interacting part of the photon dynamics is governed by the integer quantum Hall model (Fig. 1a)[15,16]. A uniform synthetic magnetic field is synthesized by using link rings to couple the neighbouring site rings such that a photon hopping from one lattice site to its neighbour experiences a position- and direction-dependent hopping phase. The tight-binding Hamiltonian describing the linear evolution of the pump, signal and idler photons in the system is given as

$$H_L = \sum_{m,n} \omega_{0\mu} a^\dagger_{m,\mu} a_{m,\mu} - J_{m,n}(a^\dagger_{m,\mu} a_{n,\mu} e^{-i\phi_{m,n}} + a^\dagger_{n,\mu} a_{m,\mu} e^{+i\phi_{m,n}}) \quad (1)$$

Here $\mu \in \{p, s, i\}$ refers to the pump, signal or idler fields, and $a^\dagger_{m,\mu}$ is the corresponding photon creation operator at a lattice site $m = (m_x, m_y)$, with frequency ω_μ. $J_{m,n}$ is the hopping rate of photons between lattice sites m, n and is non-zero only for the nearest-neighbour sites. $\phi_{m,n} = \phi m_y \delta_{m_x,n_x+1} \delta_{m_y,n_y}$ is the hopping phase between lattice sites and results in a uniform synthetic magnetic field flux ϕ per plaquette (highlighted by the dashed white line in Fig. 1a). The energy spectrum of this Hamiltonian can be probed using transmission spectroscopy. For the chosen magnetic field flux $\phi = \pi/2$, the transmission spectrum consists of two edge bands at $\omega_\mu - \omega_{0\mu} \approx \pm 1.5J$, separated by a bulk band centred at $\omega_\mu - \omega_{0\mu} \approx 0$ (Fig. 1c). The edge bands are occupied by the topological edge states, which are confined to the lattice boundary and circulate around the lattice in clockwise and anticlockwise directions,

[1]Joint Quantum Institute, NIST/University of Maryland, College Park, MD, USA. [2]IREAP/Department of Electrical and Computer Engineering, University of Maryland, College Park, MD, USA. [3]US Army Research Laboratory, Adelphi, MD, USA. [4]Department of Physics, University of Maryland, College Park, MD, USA. *e-mail: mittals@umd.edu
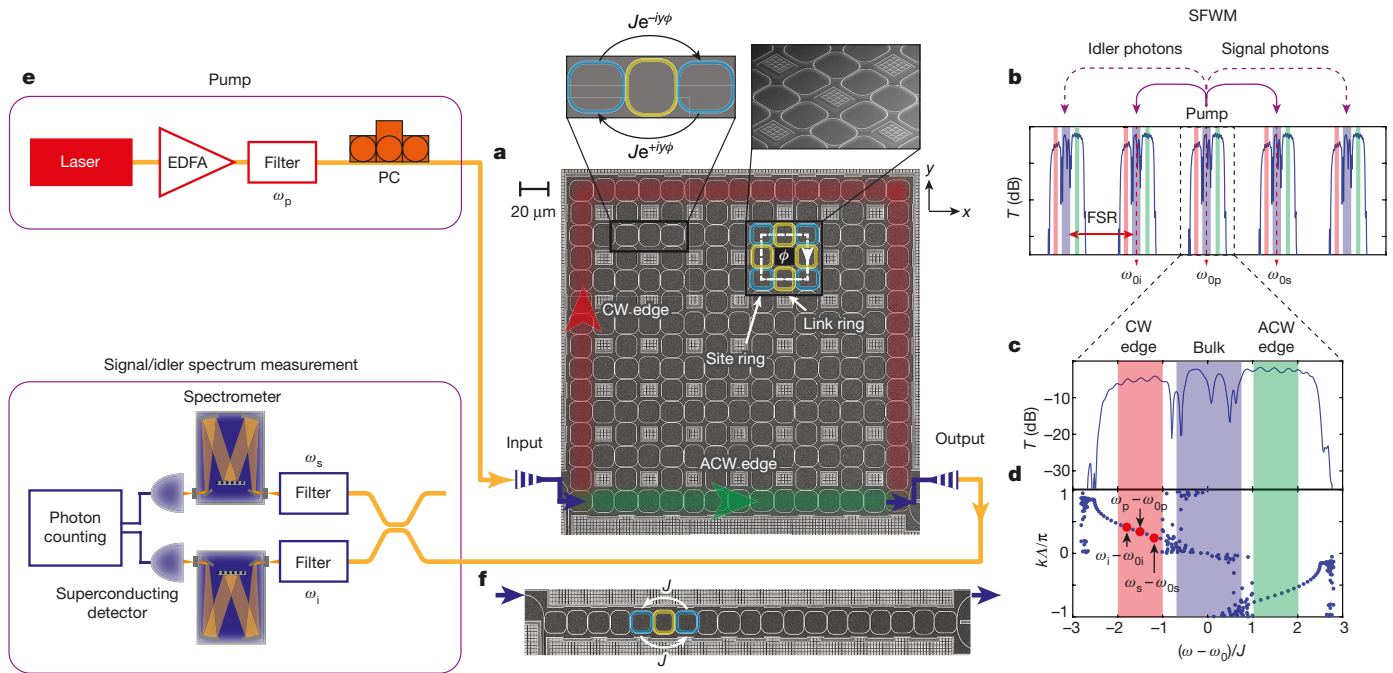
Fig. 1 | Schematic of the experimental set-up. a, Scanning electron microscope (SEM) image of an 8 × 8 lattice of site-ring resonators (cyan), coupled using link rings (yellow). Photons acquire a non-zero phase ϕ when they circulate around a plaquette of four site rings and four link rings (highlighted by the dashed white line). Insets show two site rings coupled by a link ring, and a plaquette. The paths followed by clockwise (CW) and anticlockwise (ACW) edge modes are highlighted in red and green, respectively. **b**, The transmission spectrum of the device repeats after one FSR. Correlated signal and idler photons are generated in longitudinal modes (of individual resonators) located symmetrically around the pump mode (centred at ω_{0p}). We choose the two modes one FSR above and below the pump mode, centred at frequencies ω_{0s} and ω_{0i}, for collection of signal and idler photons. **c**, Simulated transmission (T) spectrum of an 8 × 8 lattice, in a given band. Two edge bands (shaded red and green) are separated by a bulk band (shaded blue). **d**, Simulated dispersion curve showing linear dispersion for the edge modes. Here k is the photon momentum and Λ is the lattice constant such that $k\Lambda$ is the phase between two neighbouring site rings on the edge. Efficient phase-matching occurs when the pump as well as signal and idler frequencies correspond to edge modes. **e**, Schematic of the pump and the spectral measurement set-up. EDFA, erbium-doped fibre amplifier; PC, polarization controller. **f**, SEM image of a topologically trivial 1D array of ten site-ring resonators (cyan), coupled using link rings (yellow).

respectively (Fig. 1a)[16]. Furthermore, edge states are well described by a linear dispersion relation (Fig. 1d)[15,22]. In contrast, states in the bulk band occupy the bulk of the system and do not have a well-defined momentum. Note that this edge/bulk band structure repeats after every free spectral range (FSR)—that is, the frequency spacing between consecutive longitudinal modes of the individual ring resonators (Fig. 1b). Consequently, the pump, signal and idler fields can occupy different longitudinal modes with resonance frequencies denoted by $\omega_{0\mu}$.

To generate correlated photon pairs in this system, we use the third-order nonlinearity of silicon and realize SFWM. This nonlinear four-photon interaction is described by the Hamiltonian

$$H_{NL} = \eta \sum_m (a_{m,s}^\dagger a_{m,i}^\dagger a_{m,p} a_{m,p} - a_{m,p}^\dagger a_{m,p}^\dagger a_{m,s} a_{m,i}) \quad (2)$$

where η is the strength of the SFWM and depends on the material and ring waveguide properties[28,29]. The signal and idler modes are initially in the vacuum state when the input pump photons enter the system. However, the nonlinear interaction coherently adds or removes photon pairs from these vacuum modes and leads to generation of non-classical fields with intensity and spectral correlations between signal and idler photons[26]. Furthermore, because of energy conservation, correlated signal and idler photon pairs are generated in longitudinal modes (of individual resonators) located symmetrically on either side of the pump mode[28,29]. We choose signal and idler modes a single FSR above and below the pump mode, with resonance frequencies denoted by ω_{0s}, ω_{0i} and ω_{0p}, respectively (Fig. 1b). This choice allows us to effectively filter out the pump photons at the device output and also minimize the phase-mismatch arising from the waveguide and material dispersion[3,4].

In our experiment, we pump the lattice in one of the longitudinal modes using a tunable continuous-wave laser and measure the spectrum of generated photons. Figure 2a plots the linear pump transmission spectrum (see Extended Data Fig. 3 for more details) and Fig. 2b plots $\Gamma(\omega_s, \omega_p)$, the intensity of generated signal photons at frequency ω_s as we tune the pump frequency ω_p. For a continuous-wave pump, measurement of $\Gamma(\omega_s, \omega_p)$ is equivalent to a measurement of the joint-spectral intensity which is commonly used to characterize the spectral correlations between generated photons (see Extended Data Fig. 4 and refs [11,29]). First, we observe that the maximum number of photons is generated when the lattice is pumped in the clockwise edge band, at $\omega_p - \omega_{0p} \approx -1.5J$. Second, with a clockwise edge band pump, the spectrum of generated signal photons is predominantly confined to the clockwise edge band. This limited spectral distribution of signal photons can be seen more clearly with a normalized spectrum, the horizontal cross-section of $\Gamma(\omega_s, \omega_p)$, at $\omega_p - \omega_{0p} \approx -1.5J$ (Fig. 2i). Furthermore, as a consequence of energy conservation, idler photons also exhibit a similar narrow spectrum centred at the clockwise edge band: that is, $\omega_i - \omega_{0i} = 2(\omega_p - \omega_{0p}) - (\omega_s - \omega_{0s}) \approx -1.5J$ (Fig. 2j). This enhanced and spectrally limited generation of correlated photon pairs in the edge band is a result of the linear dispersion of edge modes which naturally satisfies the phase-matching criteria, and of good spatial overlap between the pump, signal and idler photons when they are confined to the lattice boundary. Our simulation results for the generated photon spectra agree well with our experimental observation (Fig. 2k). We observe a similar spectrally limited generation of correlated photons when the pump frequency is in the anticlockwise edge band (Fig. 2c–e). However, the propagation distance from the input to the output port is much shorter for the anticlockwise edge modes than for the clockwise edge modes, and therefore the intensity of generated photons is much weaker (Fig. 1a).
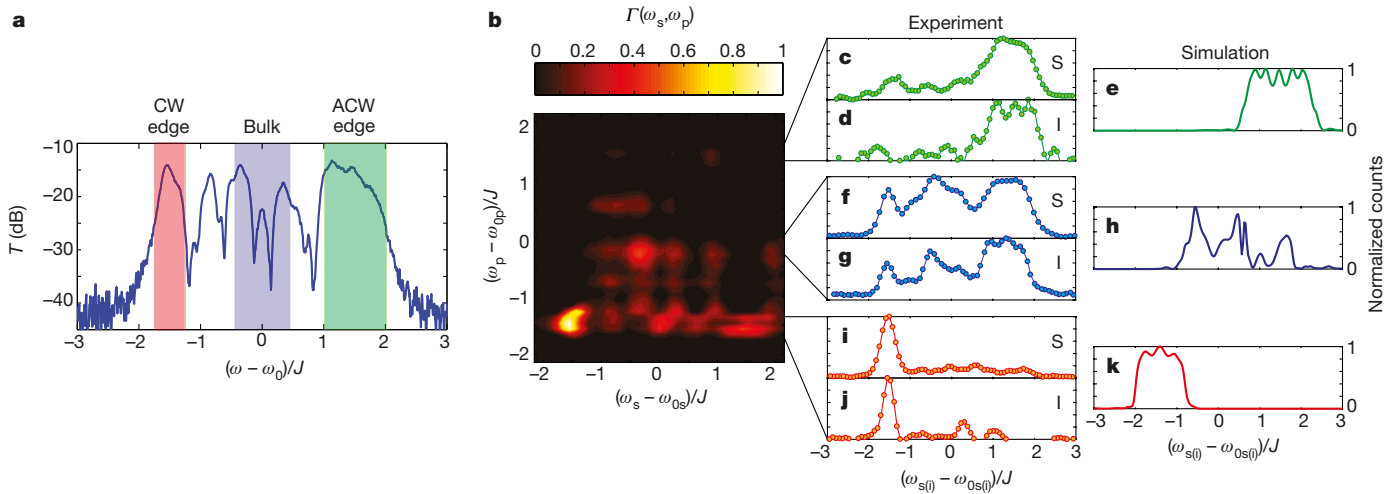
Fig. 2 | Spectral distribution of the generated photons. a, Measured transmission spectrum for an 8 × 8 lattice. The edge and bulk bands are highlighted in colour. **b**, $\Gamma(\omega_s, \omega_p)$, the intensity (normalized to unity) of generated signal photons at frequency ω_s as a function of pump frequency ω_p. The maximum number of photons are generated when the pump as well as the signal and idler frequencies are in the clockwise edge band ($\omega - \omega_0 \approx -1.5J$). **c**, Spectrum (normalized to unity) of signal (S) photons, that is, horizontal cross-section of $\Gamma(\omega_s, \omega_p)$, at $\omega_p \approx 1.5J$. With the pump in the anticlockwise edge band, the spectrum of generated signal photons is also limited to the anticlockwise edge band. **d**, Spectrum of idler (I)

photons, with the pump in the anticlockwise edge band. Because of energy conservation, idler photons are also generated predominantly in the anticlockwise edge band. **e**, Simulation results for the spectrum of generated photons match well with experimental observations. **f–h**, Corresponding results for the pump in the bulk band. The signal and idler photons are generated throughout the spectrum of the lattice. Also, the simulation results do not match the observation because of the fabrication disorder in the experimental system. **i–k**, Signal and idler spectra when the system is pumped along the clockwise edge band, again showing spectrally confined generation of photons in the edge band.

In contrast to edge modes, bulk modes do not have a well-behaved dispersion (see Fig. 1d), and their intensity distribution in the lattice changes even for very small changes in the excitation frequency[16]. Therefore, in the bulk band, there is a phase mismatch between the pump, signal and idler photons, and their spatial overlap is also limited. As a result, the SFWM efficiency is low, and photon pairs are generated throughout the transmission band of the lattice (Fig. 2f–h). Moreover, the experimental and simulation results for the bulk band pump do not match. This is because our experimental system has fabrication disorder, and the bulk band is not robust against disorder. In contrast, good agreement between the observed and simulated results for the edge states indicates their robustness against disorder.

To characterize the non-trivial nature of correlations between generated photons, we measure the second-order cross-correlation function, $g_{s,i}^{(2)}(\tau)$, which is the normalized probability of detecting signal and idler photons separated by time τ (see Methods and refs [2,5]). For two uncorrelated sources, $g^{(2)} = 1$ for all τ. In contrast, we observe a maximum $g^{(2)} \approx 80$ at $\tau = 0$ (Fig. 3a). We integrate $g_{s,i}^{(2)}(\tau)$ over the peak at $\tau = 0$ to obtain the ratio of coincidence to accidental counts (CAR), which is analogous to the signal-to-noise ratio of a source. Our source achieves a CAR ≈ 42 (Fig. 3c), higher than other similar sources using single resonators[4,5] and coupled resonators[6], for which CAR values of approximately 30 and 10 were reported, respectively. This clearly indicates that the signal and idler photons are strongly correlated: that is, the detection of a signal photon heralds the arrival of an idler photon and vice versa. Furthermore, we verified that the coincidence count rate between signal and idler photons increases as the square of the pump power (Fig. 3b) and CAR drops inversely with the coincidence rate (Fig. 3c), as expected for SFWM interaction[3–5].

Next, using a Hanbury Brown–Twiss set-up, we measure the conditional (heralded) autocorrelation function, $g_{a,h}^{(2)}(\tau)$, for signal photons, conditioned on the detection of idler photons (see Methods and refs [2,5]). Classical light sources are characterized by $g_a^{(2)}(0) \geq 1$ where the inequality holds for sources with bunched photons (such as thermal light), and $g_a^{(2)}(0) = 1$ when there are no correlations between arrival times of photons (as in lasers). Quantum light sources, such as single photons, are distinguished by $g_a^{(2)}(0) < 1$, which means that the photons are antibunched. We observe a conditional $g_{a,h}^{(2)}(0) = 0.20(8)$, which shows

antibunching and confirms that we have realized a topological source of heralded single photons (Fig. 3d).

Edge states are topologically protected, quasi-one-dimensional (1D) waveguides confined to the lattice boundary. Therefore, to benchmark the robustness of these edge channels, we compare them with the topologically trivial 1D coupled resonator optical waveguides (CROWs; Fig. 1f)[23,30]. The main advantage of CROWs over single-ring devices is that they increase the length of SFWM interaction and therefore the intensity of generated photons, without reducing their bandwidth[6,7,12]. However, unlike edge states, CROWs are not protected against disorder, which can affect the photonic mode structure (see ref. [9] and Extended
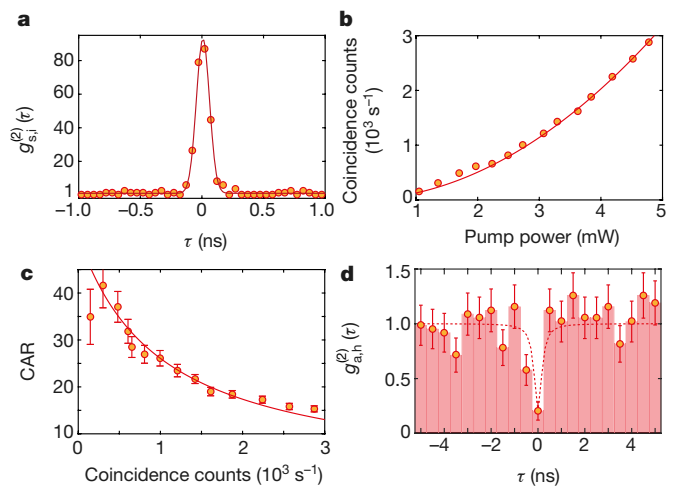

Fig. 3 | Source characterization. a, Histogram for the cross-correlation function $g_{s,i}^{(2)}(\tau)$ between signal and idler photons, with a pump power of approximately 1.4 mW. **b**, Coincidence count rate at the device output (adjusted for coupling losses), as a function of pump power. **c**, CAR as a function of the coincidence count rate. **d**, Histogram for the conditional (heralded) autocorrelation function $g_{a,h}^{(2)}$, with $g_{a,h}^{(2)}(0) = 0.20(8)$. The error bars in **b** and **c** are calculated assuming Poissonian statistics for photon counts. Solid lines are fits to the data and the dashed line is to guide the eye.
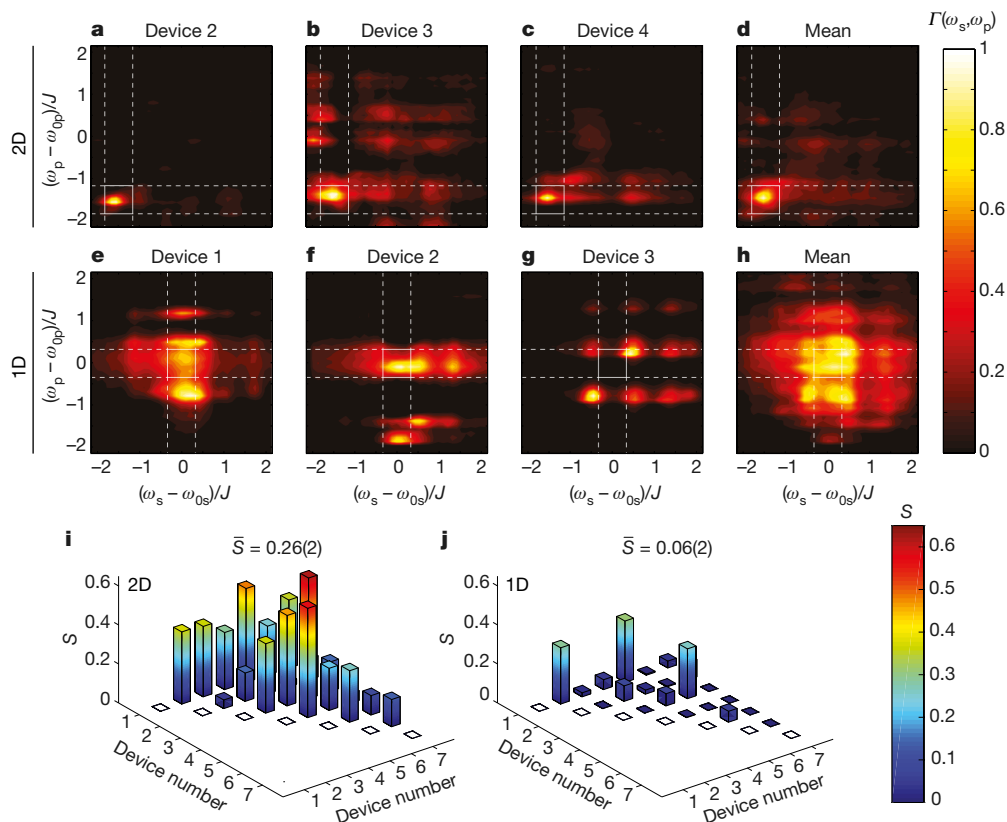
Fig. 4 | Robustness of spectral correlations between pump and signal photons. a–c, Measured $\Gamma(\omega_s, \omega_p)$, for three different 2D topological devices; **d**, the mean, measured over seven such devices (additional plots in Extended Data Fig. 1). The plots are very similar in the clockwise edge band region (marked by the solid white box), where the maximum generation of photons occurs. **e–g**, Measured $\Gamma(\omega_s, \omega_p)$, for three different 1D devices; **h**, the mean, measured over seven such devices (additional plots in Extended Data Fig. 1). There is no region of plot that is similar

across all devices. The highlighted region shows the mid-band, $|\omega_\mu - \omega_{0\mu}| < 0.25J$, where transmission is maximum (see Extended Data Fig. 2). **i, j**, Similarity (S) of $\Gamma(\omega_s, \omega_p)$ between the edge band regions of different 2D devices (**i**) and mid-band regions of 1D devices (**j**). Because of the topological robustness, edge bands achieve a much higher similarity across devices. The error in the similarity measurement for each device pair is less than 3%, and is not shown in the figure.

Data Fig. 2) and result in device-to-device variations in the spectrum of generated photons. In the following, using measurements over many devices, we show that the topological robustness of our source manifests as a robustness in the spectrum of generated photons, outperforming the trivial 1D devices.

Figure 4a–c shows $\Gamma(\omega_s, \omega_p)$, that is, the spectrum of generated photons as a function of pump frequency, for three different 2D devices, and Fig. 4d shows the mean measured over seven devices (additional data in Extended Data Fig. 1). These devices were designed to be identical, but fabrication disorder leads to random variations in the ring resonance frequencies, coupling strengths as well as hopping phases. Nevertheless, as we saw earlier, for all devices the maximum number of photons is always generated in the clockwise edge band ($\omega_s - \omega_{0s} \approx -1.5J$), with pump frequency also in the clockwise edge band ($\omega_p - \omega_{0p} \approx -1.5J$). Therefore, in the clockwise edge band region (highlighted by dashed white lines), $\Gamma(\omega_s, \omega_p)$ is very similar for all devices. In contrast to edge bands, the spectrum of generated photons in the bulk band differs from one device to the other because it is susceptible to disorder.

Figure 4e–g show similar measurements on three different topologically trivial 1D devices, and Fig. 4h shows the mean measured over seven devices. As expected, $\Gamma(\omega_s, \omega_p)$ varies markedly from device to device, meaning that the spectral correlations between the pump and the generated photons are completely random because of the randomness in the photonic mode structure induced by fabrication disorder. Therefore, given a 1D device, the spectrum of generated photons is not known a priori for any pump frequency. To further quantify and compare the spectral correlations in 2D and 1D devices, we calculate

the similarity S between $\Gamma(\omega_s, \omega_p)$ measured on two different devices (n, n'), defined as

$$S_{n,n'} = \frac{\left(\iint \sqrt{\Gamma_n \Gamma_{n'}}\, d\omega_p d\omega_s \right)^2}{\iint \Gamma_n d\omega_p d\omega_s \iint \Gamma_{n'} d\omega_p d\omega_s}$$

For the 2D devices, we chose the frequency integration interval to cover the clockwise edge band region $[-1.75J, -1.25J]$ which is robust against disorder and where the maximum number of photons are generated. For the 1D devices, we choose the mid-band region $[-0.25J, +0.25J]$ where the pump transmission is maximum (see Extended Data Fig. 2), and for a fair comparison with 2D devices, we choose the same bandwidth of $0.5J$ as we did for the edge region. These regions of interest are highlighted by white dashed lines in Fig. 4a–h. For the 2D system, the average similarity $\bar{S}$ across all devices is 0.26(2), whereas for the 1D system it is only 0.06(2) (Fig. 4i, j). These measurements demonstrate the advantage offered by the topological robustness of our 2D system in engineering the photonic mode structure and consequently the spectrum of generated photons.

The observed robustness and similarity in our 2D topological devices are remarkable given the fact that our system suffers from strong on-site potential disorder, comparable to the edge bandwidth[23]. To put our work into perspective, we numerically compare a 1D and topological 2D system, for slightly smaller disorder (Fig. 5). The average similarity for the 2D topological system is more than 90% and decreases only marginally as the system size increases. In comparison, for the 1D CROW, the similarity decreases rapidly with system size, approaching
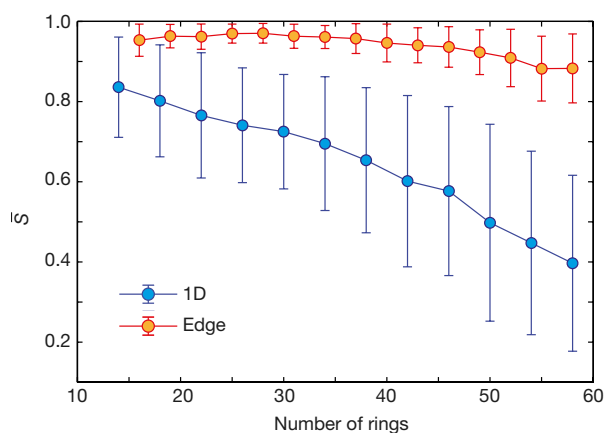
Fig. 5 | Similarity scaling as a function of device size. The simulated similarity, for moderately disordered ($V = 0.5J$) 2D and 1D systems, is shown as a function of the number of resonators travelled from the input to the output port. Because of topological protection, the 2D system achieves much higher similarity than the trivial 1D system. The results are averaged over 50 realizations of disorder. The error bars represent the standard deviation of similarity across different realizations. The solid lines are to guide the eye.

40% for 60-ring devices. The robustness of topological systems is also evident in the standard deviation of the similarity across different devices, which is considerably smaller than that of 1D CROWs. This indicates that with moderate disorder, high-visibility two-photon and multi-photon interference[11] should be possible with photons generated by different 2D topological sources.

In summary, we have demonstrated a topological source of quantum correlated photon pairs in which the spectral correlations are robust against fabrication disorder. This is a step towards on-chip, scalable sources of heralded and entangled photons with identical spectra, for applications in quantum information processing and quantum communications. Although this demonstration uses devices with relatively high propagation loss (of the order of 1 dB cm^{-1}), recent developments of ultra-low-loss photonic platforms (of the order of 10^{-3} dB cm^{-1})[31,32] could lead to orders of magnitude improvement in the source brightness. Moreover, such low-loss platforms would enable quantum-limited topological amplifiers, for which the four-wave mixing gain is required to exceed the propagation losses[26].

On a more fundamental level, we have demonstrated a robust route to manipulating the structure and vacuum fluctuations of the electromagnetic modes by using topological photonics. This could have far-reaching implications in engineering light–matter interactions in the quantum regime. We expect intriguing consequences to emerge from application of these ideas to physical phenomena such as spontaneous emission, super- and sub-radiance, and the Casimir effect.

Online content

Any methods, additional references, Nature Research reporting summaries, source data, statements of data availability and associated accession codes are available at https://doi.org/10.1038/s41586-018-0478-3.

1. Shields, A. J. Semiconductor quantum light sources. *Nat. Photon.* **1**, 215–223 (2007).
2. Eisaman, M. D., Fan, J., Migdall, A. & Polyakov, S. V. Single-photon sources and detectors. *Rev. Sci. Instrum.* **82**, 071101 (2011).
3. Sharping, J. E. et al. Generation of correlated photons in nanoscale silicon waveguides. *Opt. Express* **14**, 12388–12393 (2006).
4. Clemmen, S. et al. Continuous wave photon pair generation in silicon-on-insulator waveguides and ring resonators. *Opt. Express* **17**, 16558–16570 (2009).
5. Förtsch, M. et al. A versatile source of single photons for quantum information processing. *Nat. Commun.* **4**, 1818 (2013).
6. Davanço, M. et al. Telecommunications-band heralded single photons from a silicon nanophotonic chip. *Appl. Phys. Lett.* **100**, 261104 (2012).
7. Kumar, R., Ong, J. R., Savanier, M. & Mookherjea, S. Controlling the spectrum of photons generated on a silicon nanophotonic chip. *Nat. Commun.* **5**, 5489 (2014).
8. Topolancik, J., Ilic, B. & Vollmer, F. Experimental observation of strong photon localization in disordered photonic crystal waveguides. *Phys. Rev. Lett.* **99**, 253901 (2007).
9. Mookherjea, S., Park, J. S., Yang, S.-H. & Bandaru, P. R. Localization in silicon nanophotonic slow-light waveguides. *Nat. Photon.* **2**, 90–93 (2008).
10. Sapienza, L. et al. Cavity quantum electrodynamics with anderson-localized modes. *Science* **327**, 1352–1355 (2010).
11. Spring, J. B. et al. Chip-based array of near-identical, pure, heralded single-photon sources. *Optica* **4**, 90–96 (2017).
12. Morichetti, F. et al. Travelling-wave resonant four-wave mixing breaks the limits of cavity-enhanced all-optical wavelength conversion. *Nat. Commun.* **2**, 296 (2011).
13. Lu, L., Joannopoulos, J. D. & Soljačić, M. Topological photonics. *Nat. Photon.* **8**, 821–829 (2014).
14. Wang, Z., Chong, Y., Joannopoulos, J. D. & Soljačić, M. Observation of unidirectional backscattering-immune topological electromagnetic states. *Nature* **461**, 772–775 (2009).
15. Hafezi, M., Demler, E. A., Lukin, M. D. & Taylor, J. M. Robust optical delay lines with topological protection. *Nat. Phys.* **7**, 907–912 (2011).
16. Hafezi, M., Mittal, S., Fan, J., Migdall, A. & Taylor, J. M. Imaging topological edge states in silicon photonics. *Nat. Photon.* **7**, 1001–1005 (2013).
17. Rechtsman, M. C. et al. Photonic Floquet topological insulators. *Nature* **496**, 196–200 (2013).
18. Chen, W.-J. et al. Experimental realization of photonic topological insulator in a uniaxial metacrystal waveguide. *Nat. Commun.* **5**, 5782 (2014).
19. Cheng, X. et al. Robust reconfigurable electromagnetic pathways within a photonic topological insulator. *Nat. Mater.* **15**, 542–548 (2016).
20. Kraus, Y., Lahini, Y., Ringel, Z., Verbin, M. & Zilberberg, O. Topological states and adiabatic pumping in quasicrystals. *Phys. Rev. Lett.* **109**, 106402 (2012).
21. Hafezi, M. Measuring topological invariants in photonic systems. *Phys. Rev. Lett.* **112**, 210405 (2014).
22. Mittal, S., Ganeshan, S., Fan, J., Vaezi, A. & Hafezi, M. Measurement of topological invariants in a 2D photonic system. *Nat. Photon.* **10**, 180–183 (2016).
23. Mittal, S. et al. Topologically robust transport of photons in a synthetic gauge field. *Phys. Rev. Lett.* **113**, 087403 (2014).
24. St-Jean, P. et al. Lasing in topological edge states of a one-dimensional lattice. *Nat. Photon.* **11**, 651–656 (2017).
25. Bahari, B. et al. Nonreciprocal lasing in topological cavities of arbitrary geometries. *Science* **358**, 636–640 (2017).
26. Peano, V., Houde, M., Marquardt, F. & Clerk, A. A. Topological quantum fluctuations and traveling wave amplifiers. *Phys. Rev. X* **6**, 041026 (2016).
27. Shi, T., Kimble, H. J. & Cirac, J. I. Topological phenomena in classical optical networks. *Proc. Natl Acad. Sci. USA* **114**, E8967–E8976 (2017).
28. Chen, J., Levine, Z. H., Fan, J. & Migdall, A. L. Frequency-bin entangled comb of photon pairs from a silicon-on-insulator micro-resonator. *Opt. Express* **19**, 1470–1483 (2011).
29. Ong, J. R. & Mookherjea, S. Quantum light generation on a silicon chip using waveguides and resonators. *Opt. Express* **21**, 5171–5181 (2013).
30. Yariv, A., Xu, Y., Lee, R. K. & Scherer, A. Coupled-resonator optical waveguide: a proposal and analysis. *Opt. Lett.* **24**, 711–713 (1999).
31. Bauters, J. F. et al. Ultra-low-loss high-aspect-ratio Si$_3$N$_4$ waveguides. *Opt. Express* **19**, 3163–3174 (2011).
32. Moss, D. J., Morandotti, R., Gaeta, A. L. & Lipson, M. New CMOS-compatible platforms based on silicon nitride and hydex for nonlinear optics. *Nat. Photon.* **7**, 597–607 (2013).

Author contributions S.M. and M.H. conceived the idea. S.M. performed the numerical simulations and the experimental measurements. E.A.G. contributed to source characterization. M.H. supervised the project. All authors contributed to analysing the data and writing the manuscript.

METHODS

Simulation of signal/idler spectra. In this section, we describe the method used to simulate the spectrum of the generated signal and idler photons in response to a strong pump field. We follow the approach described in refs [28,29]. The linear, uncoupled evolution of the pump, signal and idler fields is governed by the Hamiltonian H_L, given by equation (1) and repeated here for convenience, as

$$H_L = \sum_{m,n} \omega_{0\mu} a^\dagger_{m,\mu} a_{m,\mu} - J_{m,n}(a^\dagger_{m,\mu} a_{n,\mu} e^{-i\phi_{m,n}} + a^\dagger_{n,\mu} a_{m,\mu} e^{+i\phi_{m,n}})$$

where $\mu \in \{p, s, i\}$ corresponds to the pump, signal or idler fields. The nonlinear SFWM process which couples the pump, signal and idler fields is described by the Hamiltonian (equation (2))

$$H_{NL} = \eta \sum_m (a^\dagger_{m,s} a^\dagger_{m,i} a_{m,p} a_{m,p} - a^\dagger_{m,p} a^\dagger_{m,p} a_{m,s} a_{m,i})$$

Note that this Hamiltonian is local in lattice site index m. We assume that the pump field is much stronger than the signal and idler fields and therefore the evolution of the pump field is very well described by the linear Hamiltonian. However, the pump field depletes because of the intrinsic waveguide scattering losses (κ_{in}), which we include in our simulation. Using the input–output formalism and the rotating-wave approximation, we can write the coupled equations describing the steady-state pump field amplitudes, for frequency ω_p, as

$$-i\omega_p a_{m,p} = i[H_L, a_{m,p}] - \kappa_{in} a_{m,p} - (\delta_{m,I} + \delta_{m,O})\kappa_{ex} a_{m,p} - \delta_{m,I}\sqrt{2\kappa_{ex}} a_{in,p} \quad (3)$$

Here κ_{ex} is the coupling strength of the lattice to input/output waveguides and $a_{in,p}$ is the input pump field. The input and output waveguides are coupled to the lattice at sites indexed by I, O.

Given the pump field amplitudes calculated using equation (3), we can write the coupled equations describing the steady-state signal and idler fields amplitudes in the lattice as

$$-i\omega_\mu a_{m,\mu} = i[H_L + H_{NL}, a_{m,\mu}] - \kappa_{in} a_{m,\mu} - (\delta_{m,I} + \delta_{m,O})\kappa_{ex} a_{m,\mu} - \delta_{m,I}\sqrt{2\kappa_{ex}} a_{in,\mu}$$

where $\mu \in \{s, i\}$. These equations include the nonlinear FWM interaction Hamiltonian of equation (2) which couples the signal and idler fields to the pump fields. Also, for a particular choice of frequencies ω_p and ω_s, energy conservation fixes the idler frequency ω_i.

Using these coupled equations for the pump, signal and idler frequencies, we calculate their field amplitudes in the lattice. Then the signal/idler fields at the output of the lattice are calculated using the input–output formalism as

$$a_{out,\mu} = \sqrt{2\kappa_{ex}} a_{O,\mu}$$

where O is the index denoting the lattice output site. We can now define the spectral correlation function (SCF) $\Gamma(\omega_s, \omega_p) = |a_{out,s}|^2$. This is essentially the spectrum of generated signal photons as a function of pump frequency. Note that because of the energy conservation relation $2\omega_p = \omega_s + \omega_i$, this SCF fully characterizes the spectral correlations of the SFWM process. In other words, using $\Gamma(\omega_s, \omega_p)$, we can easily calculate $\Gamma(\omega_s, \omega_i)$, the joint-spectral intensity of the signal and idler photons.

Experimental set-up. The devices used in this experiment were fabricated using CMOS-compatible silicon-on-insulator technology. The ring resonator waveguides are approximately 510 nm in width and 220 nm in height, and at telecom wavelengths (approximately 1,550 nm) support only a single mode with transverse electric field. The coupling strength J between the resonators was measured to be 32(1) GHz and the FSR was about 1,035 GHz. The on-site disorder potential V, which is a result of the different ring resonance frequencies, was estimated to be 27.5 GHz, and the disorder on the hopping phase was 0.1. Additional details of the fabrication process and disorder characterization are available in refs [16,23].

To generate correlated photons using the SFWM process, we pumped the lattice with a telecom band, tunable, continuous-wave laser. The output of the laser was amplified using an erbium-doped fibre amplifier (EDFA), and a tunable bandpass filter was used to cut down the spontaneous emission generated during amplification. The pump was coupled to the lattice using grating couplers, with a coupling loss of about 5 dB per coupler. At the output of the lattice, tunable bandpass filters were used to remove the pump band, with a rejection exceeding 120 dB. The signal and idler photons were collected from bands separated by ± 1 FSR from the pump band, respectively. To measure the spectrum of generated signal and idler photons, we used two monochromators with a frequency resolution of about 6 GHz along with two superconducting nanowire single photon detectors (PhotonSpot). The second-order correlation function measurements were done with a time-correlated single photon counting system (HydraHarp).

Source characterization. We use second-order correlation measurements to characterize our source [2,5]. The temporal correlations between signal and idler photons are analysed using the cross-correlation function $g^{(2)}_{s,i}(\tau)$ which is given as

$$g^{(2)}_{s,i}(\tau) = \frac{P_{s,i}(\tau)}{P_s P_i}$$

Here $P_{s,i}$ is the probability of detecting a signal photon at time t followed by the detection of an idler photon in the time interval $[t + \tau - \tau_c/2, t + \tau + \tau_c/2]$, and τ_c (here 50 ps) is the coincidence time-window. P_s and P_i are the probabilities of detecting individual signal or idler photons, and the product $P_s P_i$ is the probability of detecting accidental coincidences. We observe that $g^{(2)}_{s,i}(\tau) \approx 80$ around $\tau = 0$, which implies that the generation of signal and idler photons is strongly correlated. The mean of $g^{(2)}_{s,i}(\tau)$ around $\tau = 0$ corresponds to actual coincidence counts, whereas its mean at $|\tau| \gg 0$ corresponds to accidental counts ($P_s P_i$). Their ratio (CAR) is commonly used as a measure of the signal-to-noise ratio of a source. We measure a maximum CAR ≈ 42 when $g^{(2)}_{s,i}$ is averaged over 300 ps (the width of the correlation peak).

The quantum nature of a source can be demonstrated by the second-order autocorrelation function $g^{(2)}_a(\tau)$, which is a measure of antibunching of photons [2,5]. Quantum sources are distinguished by $g^{(2)}_a(0) < 1$, which suggests that the normalized probability of getting two simultaneous photons is low. In the case of correlated photon pairs, the quantum nature is revealed when we measure the conditional autocorrelation function $g^{(2)}_{a,h}(\tau)$ for signal photons heralded (conditioned) by the detection of idler photons. For this measurement, we use the Hanbury Brown–Twiss (HBT) set-up in which we place a beam-splitter in the path of signal photons, and the outputs of the beam-splitter are connected to two detectors (s_1 and s_2). The idler photons impinge on a third detector (i) which heralds the arrival of signal photons. Then the conditional autocorrelation function $g^{(2)}_{a,h}(\tau)$ for signal photons, conditioned on the detection of idler photons, is defined as

$$g^{(2)}_{a,h}(\tau) = \frac{P_{s_1,s_2,i}(\tau)}{P_{s_1,i} P_{s_2,i}}$$

Here $P_{s_1,s_2,i}(\tau)$ is the probability of detecting two heralded signal photons separated by a time τ and $P_{s_{1,2},i}$ is the probability of detecting individual heralded signal photons. These probabilities are normalized by the probability of idler (heralding) photons. Therefore, $g^{(2)}_{a,h}(0) = 0 = P_{s_1,s_2,i}(0)$ indicates that the probability of having two pairs of signal and idler photons at the same time is zero. We measure $g^{(2)}_{a,h}(0) = 0.20(8)$, which is a signature of a good source of heralded single photons.

Data availability. The data that support the findings of this study are available from the corresponding author on reasonable request.
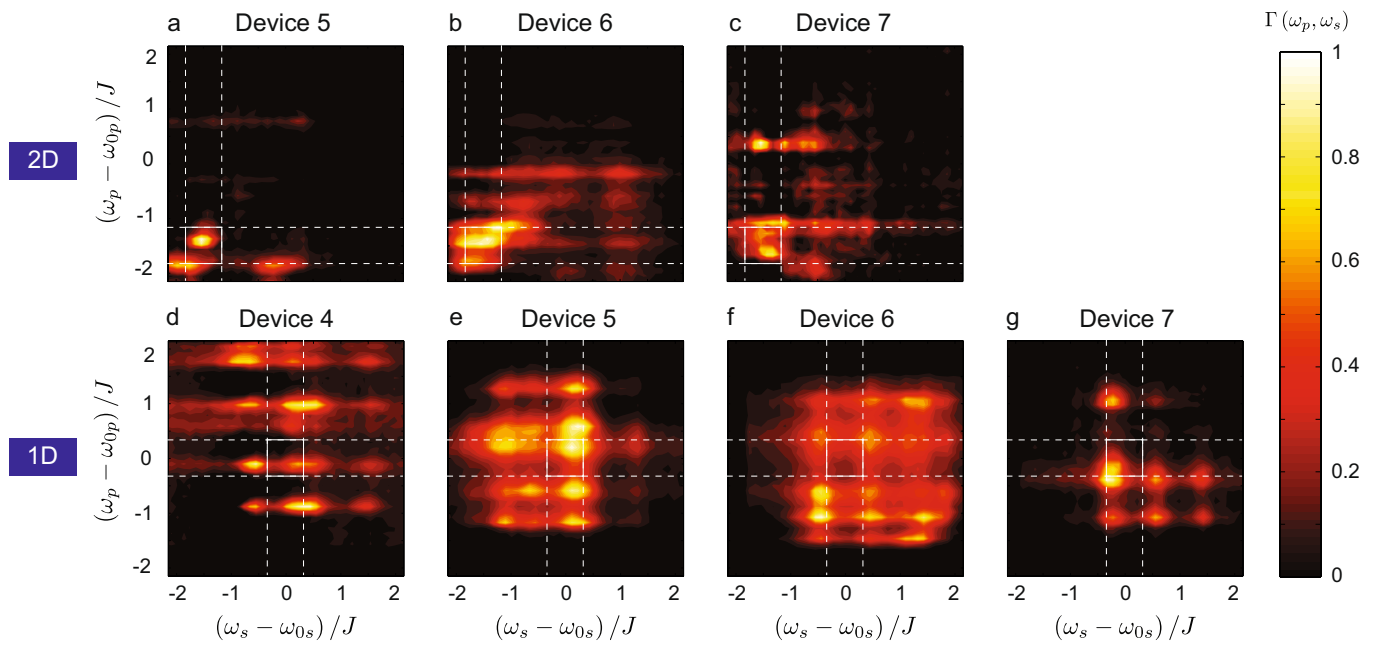
Extended Data Fig. 1 | Spectral correlations. a–c, Measured $\Gamma(\omega_s, \omega_p)$ on three different 2D devices; **d–g**, measured $\Gamma(\omega_s, \omega_p)$ on four different 1D devices, in addition to those presented in Fig. 3. Clockwise edge bands for the 2D devices and mid-band for the 1D devices are highlighted.
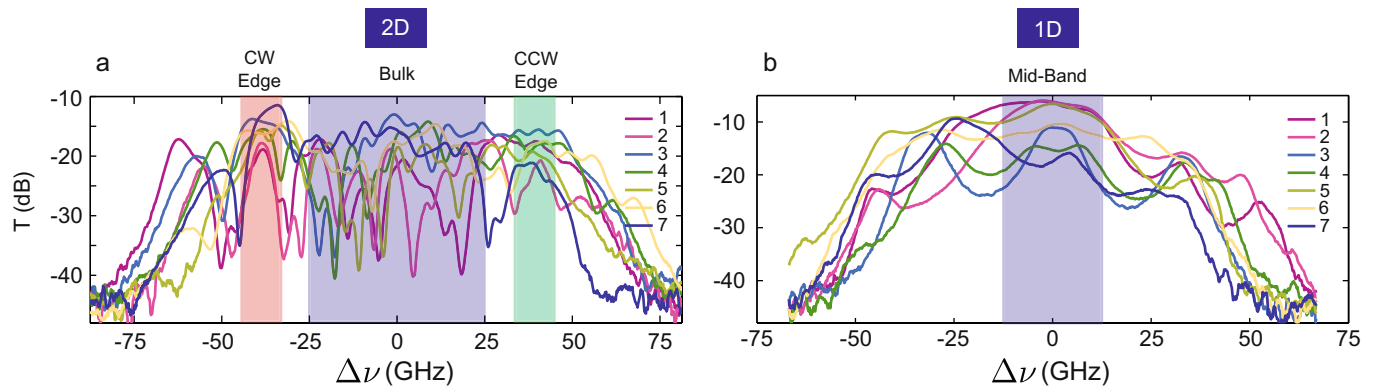
Extended Data Fig. 2 | Transmission spectra of 2D and 1D devices. **a**, **b**, Measured transmission spectra for (**a**) different 2D and (**b**) different 1D devices. The shaded regions highlight the edge and the bulk bands for the 2D system and the mid-band for the 1D system. For the 2D devices, the clockwise and the anticlockwise edge bands show reduced variations in the transmission compared with that in the bulk band. These spectra have been shifted along the frequency axis to superpose them, using an algorithm based on transmission and delay measurements, as detailed in ref. [23].
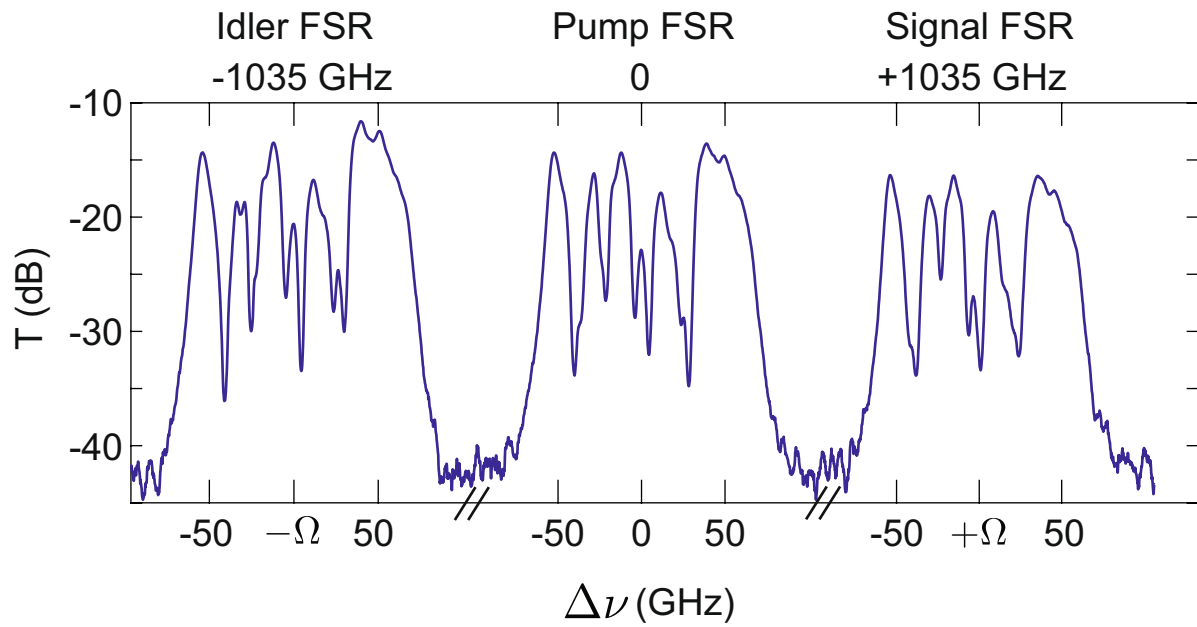
Extended Data Fig. 3 | Transmission spectrum of a 2D device across three FSRs. Measured transmission spectrum in the pump, signal and idler FSRs, corresponding to Fig. 2. $\Delta\nu$ is the frequency relative to the longitudinal mode resonance, and Ω is the FSR. The shape of the transmission spectrum in these FSRs is almost identical. The small variation in the overall transmission across bands is mainly because of the frequency response of the grating couplers.
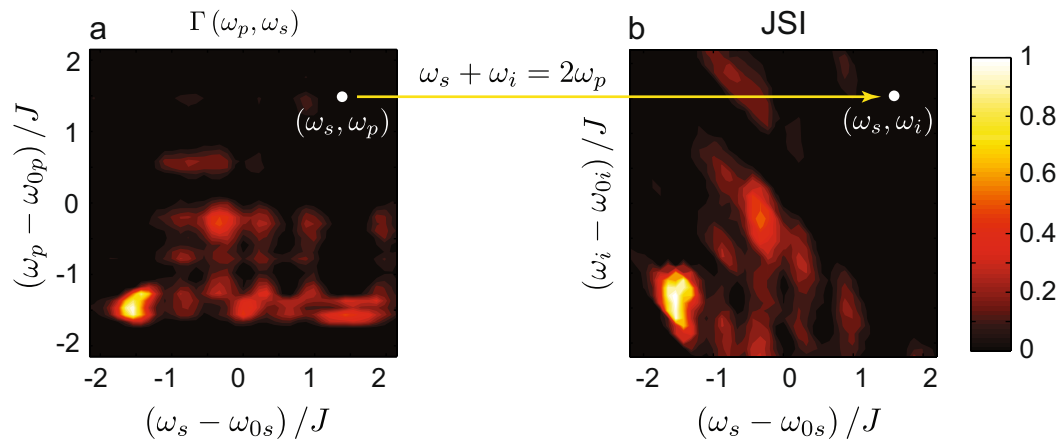
Extended Data Fig. 4 | Joint spectral intensity. a, The measured $\Gamma(\omega_s, \omega_p)$ (see Fig. 2): that is, the intensity of generated signal photons at frequency ω_s as a function of pump frequency, ω_p. Each point on this plot represents a particular ω_s and ω_p. Using energy conservation, we can calculate the corresponding idler frequency at each point as $\omega_i = 2\omega_p - \omega_s$. Therefore, we can easily rescale the y axis of the plot and calculate the joint-spectral intensity (JSI; see refs [11,29]) between the signal and idler frequencies, as shown in **b**. Note that this rescaling works only for a continuous-wave pump because for a pulsed pump source, the above energy conservation relation holds only up to the spectral bandwidth of the pump, signal and idler photons. Also, this measurement inherently assumes that the generated signal and idler photons are correlated. Using CAR and direct measurements of the signal and idler spectra (in Figs. 2, 3), we verified that the signal and idler photons are indeed correlated. The main advantage of such a spectral correlation measurement between the pump and the signal (or idler) photons is that it is fast and, for a continuous-wave pump, is equivalent to the JSI measurement.